GEOPHYSICS, VOL. 81, NO. 5 (SEPTEMBER-OCTOBER 2016); P. S383–S398, 21 FIGS.
10.1190/GEO2015-0704.1

Scalar and vector imaging based on wave mode decoupling for elastic reverse time migration in isotropic and transversely isotropic media

Chenlong Wang[1], Jiubing Cheng[2], and Børge Arntsen[3]

ABSTRACT

Recording P- and S-wave modes acquires more information related to rock properties of the earth's interior. Elastic migration, as a part of multicomponent seismic data processing, potentially offers a great improvement over conventional acoustic migration to create a spatial image of some medium properties. In the framework of elastic reverse time migration, we have developed new scalar and vector imaging conditions assisted by efficient polarization-based mode decoupling to avoid crosstalk among the different wave modes for isotropic and transversely isotropic media. For the scalar imaging, we corrected polarity reversal of zero-lag PS images using the local angular attributes on the fly of angle-domain imaging. For the vector imaging, we naturally used the polarization information in the decoupled single-mode vector fields to automatically avoid the polarity reversal and to estimate the local angular attributes for angle-domain imaging. Examples of increasing complexity in 2D and 3D cases found that the proposed approaches can be used to obtain a physically interpretable image and angle-domain common-image gather at an acceptable computational cost. Decoupling and imaging the 3D S-waves involves some complexity, which has not been addressed in the literature. For this reason, we also attempted at illustrating the physical contents of the two separated S-wave modes and their contribution to seismic full-wave imaging.

INTRODUCTION

Due to the elastic nature of the earth media, seismic waves propagate through it as a superposition of P- and S-wave modes. An S-wave passing through an anisotropic medium splits into two mutually orthogonal waves. In general, the P-wave and the two S-waves in anisotropic materials do not polarize parallel or perpendicular to the wave vectors; therefore, they are called quasi-P (qP) and quasi-S (qS) waves. Unlike the well-behaved qP mode, the two qS modes do not consistently polarize as a function of the propagation direction and thus cannot be designated as qSV- and qSH-waves, except in transversely isotropic (TI) media (Winterstein, 1990; Crampin, 1991). Recording all wave modes through multicomponent seismic acquires more information related to rock properties and thus provides better subsurface imaging and more accurate estimation of reservoir characteristics (Stewart et al., 2002).

Most of the approaches proposed in the literature perform elastic imaging by Kirchhoff migration (Kuo and Dai, 1984) or reverse time migration (RTM) (Chang and McMechan, 1986; Yan and Sava, 2008). The ray-based elastic Kirchhoff method is efficient but it is limited when dealing with many wave-related phenomena (Gray et al., 2001). RTM is a well-established migration technique that creates a spatial image of the subsurface. Based on the full-wave equation, it is free from high-frequency assumption (as Kirchhoff migration) and dip-angle limitation (as one-way wave-equation migration). Early attempts at elastic RTM (ERTM) apply the excitation-time imaging condition to the reconstructed wavefields, in which the arrival times from the source to the image point are calculated by ray tracing (Chang and McMechan, 1986). The standard RTM procedure generally applies crosscorrelation (or deconvolution) imaging condition with zero lag in space and time (Claerbout, 1985) to the reconstructed source and receiver wavefields in the subsurface. For ERTM, however, a simple component-by-component crosscorrelation leads to the artifacts caused by crosstalk among the unseparated wave modes, which makes it difficult to interpret the images in terms

Manuscript received by the Editor 20 December 2015; revised manuscript received 23 May 2016; published online 11 August 2016.
[1]Tongji University, School of Ocean and Earth Science, Shanghai, China. E-mail: clwang88@gmail.com.
[2]Tongji University, State Key Laboratory of Marine Geology, Shanghai, China. E-mail: cjb1206@tongji.edu.cn.
[3]Norwegian University of Science and Technology, Department of Petroleum Engineering and Applied Geophysics, Trondheim, Norway. E-mail: borge.arntsen@ntnu.no.

of pure modes (e.g., PP or PS) reflections. Therefore, Yan and Sava (2008) suggest using a set of imaging conditions that combines the various incident and reflected potentials separated by the Helmholtz decomposition.

Recently, there has been a renewed interest in common-image gathers (CIGs) and various approaches have been proposed to compute angle-domain CIGs for RTM. These techniques can be categorized into two main classes: postimaging and preimaging. In general, the postimaging algorithms based on the extended imaging condition (Biondi and Symes, 2004; Sava and Fomel, 2006) are more attractive from a computational perspective, whereas the preimaging algorithms that estimate the local directions of the extrapolated wavefields before or at the time of applying the imaging condition (Yoon and Marfurt, 2006; Xu et al., 2011; Yan and Xie, 2012; Wang and McMechan, 2015) are considered more flexible (Vyas et al., 2011). An available scheme in preimaging category is to decompose the normal zero-lag RTM image into angle/azimuth bins according to the local propagation direction obtained from the Poynting vector (Yoon and Marfurt, 2006; Dickens and Winbow, 2011). It is important to note that the Poynting vector gives the direction of energy propagation. Therefore, it points in the direction of the group-velocity vector in anisotropic media. Yan and Xie (2012) provide a method to construct angle gathers in isotropic elastic media based on the local Fourier transform, which is considered very accurate. Zhang and McMechan (2011b) and Wang and McMechan (2015) propose a method to estimate the incident P-wave direction based on the wavefields polarization that derived from the separation solution of Ma and Zhu (2003) for isotropic media. Zhang and McMechan (2011a) also extend it to 2D VTI (transversely isotropic with a vertical symmetry axis) media by taking the qP-wave polarization direction that contains in the vector qP-wavefields as the phase direction.

However, these efforts still have many limitations for angle-domain ERTM in anisotropic media. First, wave mode separation in heterogeneous anisotropic media is prohibitively expensive, because the operators involved are dependent on the medium parameters, and thus, the operators are not stationary (Yan and Sava, 2009). This is why Zhang and McMechan (2011b) choose to apply the excitation imaging condition instead of the crosscorrelation imaging condition to the single mode wavefield separated by a local Fourier transform operation in their ERTM algorithm for 2D VTI media. To map the RTM images into angle bins efficiently, they ignore the deviation between the polarization and the phase directions of qP-wave in VTI media. In fact, in an anisotropic medium, it is necessary to distinguish between the group (or the polarization) direction and the phase direction (Tsvankin et al., 2001), because reflection properties are governed by the phase angle (Dickens and Winbow, 2011; McGarry and Qin, 2013; Wang et al., 2014).

Our motivation of this paper is to study new imaging conditions of ERTM using polarization-based wave mode decoupling for isotropic and TI media. We propose a scalar imaging condition and a vector imaging condition that apply to the decoupled scalar and vector wavefields, respectively. For clarity, we call the scalar (or scalarized) wavefields involved imaging condition scalar imaging and the vector wavefields involved imaging condition vector imaging in this paper. Both imaging conditions are extended to get incident phase angle-domain CIGs according to the group or polarization direction of the decoupled wavefields. Synthetic examples demonstrate the validity of the proposed approaches for simple and complex TI models.

ELASTIC WAVEFIELD DECOUPLING

The RTM algorithm consists of two consecutive steps: the wavefields reconstruction and the application of an imaging condition. For prestack depth migration, source and receiver wavefields must be reconstructed at all locations in the subsurface, given the actual seismic recordings and source function on the acquisition surface. The imaging condition evaluates the match between wavefields reconstructed from the sources and receivers. For ERTM, a simple component-by-component crosscorrelation imaging condition leads to the artifacts caused by crosstalk among the unseparated wave modes. To obtain physically interpretable images, wave mode decoupling before the application of the imaging condition is essential for ERTM (Dellinger and Etgen, 1990; Yan and Sava, 2008). In general, wave mode decoupling in elastic media can be classified into three categories: the Helmholtz(-like) decomposition, polarization-based scalar separation, and polarization-based vector decomposition (Zhang and McMechan, 2010).

The Helmholtz(-like) decomposition

In isotropic media, the separation of the elastic far-field displacement wavefields $\mathbf{u} = \{u_x, u_y, u_z\}$ by the divergence and curl operators is given as (Aki and Richards, 2002):

$$P(\mathbf{x}) = \nabla \cdot \mathbf{u}(\mathbf{x}), \qquad \mathbf{S}(\mathbf{x}) = \nabla \times \mathbf{u}(\mathbf{x}), \tag{1}$$

where $\mathbf{x} = (x, y, z)$ represents the spatial coordinate and $\nabla = (\partial/\partial x, \partial/\partial y, \partial/\partial z)$. The separated P and $\mathbf{S}$ are scalar and vector potential wavefields, respectively. Equation 1 has the wavenumber-domain equivalent form:

$$\tilde{P}(\mathbf{k}) = i\mathbf{k} \cdot \tilde{\mathbf{u}}(\mathbf{k}), \qquad \tilde{\mathbf{S}}(\mathbf{k}) = i\mathbf{k} \times \tilde{\mathbf{u}}(\mathbf{k}), \tag{2}$$

where $i = \sqrt{-1}$, $\mathbf{k} = (k_x, k_y, k_z)$ represents a vector parallel to the direction of wave propagation (namely wave vector). The variable with "$\sim$" denotes the corresponding wavefield in the wavenumber domain. Dellinger and Etgen (1990) extend the Helmholtz decomposition into anisotropic media through substituting the wave vector $\mathbf{k}$ by the qP-wave polarization vector $\mathbf{a}_P$ yielding

$$q\tilde{P}(\mathbf{k}) = i\mathbf{a}_P(\mathbf{k}) \cdot \tilde{\mathbf{u}}(\mathbf{k}), \qquad q\tilde{\mathbf{S}}(\mathbf{k}) = i\mathbf{a}_P(\mathbf{k}) \times \tilde{\mathbf{u}}(\mathbf{k}). \tag{3}$$

The polarization vector of the qP-wave can be obtained by solving the Christoffel equation (see Appendix A). Note that the Helmholtz (-like) decomposition separates the original wavefield into a scalar qP-wavefield and a vector qS-wavefield, and the separated qS-wave contains all non-qP parts of the elastic wavefields.

Polarization-based decoupling

The polarization orthogonality among the wave modes intrinsically provides a general framework to decouple the far-field elastic body waves (Dellinger and Etgen, 1990; Yan and Sava, 2009; Zhang and McMechan, 2010). For TI media, the S-waves can be designated as qSV-wave (polarizes in the symmetry-axis planes) and qSH-wave (polarizes in the isotropy planes) (Winterstein, 1990). Based on the polarization information, the original elastic wavefield can be decoupled into either scalar or vector wavefield of the corresponding wave mode.

For instance, in the wavenumber domain, a single wave mode can be separated by projecting the wavefields onto the direction in which it polarizes:

$$\tilde{u}_m(\mathbf{k}) = i\bar{\mathbf{a}}_m(\mathbf{k}) \cdot \tilde{\mathbf{u}}(\mathbf{k}), \tag{4}$$

where $u_m(m = \{\mathrm{qP}, \mathrm{qSV}, \mathrm{qSH}\})$ represents the separated scalar wavefield; $\bar{\mathbf{a}}_m(\mathbf{k})$ stands for the unit polarization vector of different wave modes, which is $\mathbf{a}_m(\mathbf{k})$ normalized by $|\mathbf{a}_m(\mathbf{k})|$ and thus is dimensionless. Unlike the Helmholtz(-like) decomposition, the polarization-based separation decouples the shear wavefield into two scalar fields.

Vector decomposition aims at separating the elastic wavefields into vector fields of each mode. For example, we can achieve this by using the following polarization-based vector decomposition:

$$\tilde{\mathbf{u}}_m(\mathbf{k}) = \bar{\mathbf{a}}_m(\mathbf{k})[\bar{\mathbf{a}}_m(\mathbf{k}) \cdot \tilde{\mathbf{u}}(\mathbf{k})], \tag{5}$$

for homogeneous media in the wavenumber domain (Zhang and McMechan, 2010). Note that the above decomposition honors the following linear superposition relation:

$$\tilde{\mathbf{u}}(\mathbf{k}) = \tilde{\mathbf{u}}_{\mathrm{qP}}(\mathbf{k}) + \tilde{\mathbf{u}}_{\mathrm{qSV}}(\mathbf{k}) + \tilde{\mathbf{u}}_{\mathrm{qSH}}(\mathbf{k}) \tag{6}$$

for TI media. The decomposed single-mode wavefields have the same amplitude, polarization, phase, physical meaning, and the units as those in the original elastic wavefields (Zhang and McMechan, 2010).

To solve the equations 4 and 5, the calculation of polarization vector of each mode is required. The determination of the polarization directions is based on solving the Christoffel equation and using the polarization orthogonality among different wave modes (Appendix A). The qSV- and qSH-waves are restricted to polarize in symmetry axis plane and isotropy plane, respectively. For general TI media, the direction of the symmetry axis may be not along the vertical axis and spatially varies with wave propagation. Therefore, qSH-waves may not horizontally polarize and qSV-waves may not polarize in the vertical plane. These two S-waves own different phase velocities except in the directions of shear singularities. As investigated by Crampin and Yedlin (1981), a TI material only has the line and kiss singularities. A line singularity occurs only at a fixed angle from the symmetry axis and causes no distortion of phase velocity surfaces or polarization phenomena, whereas a kiss singularity occurs only along the symmetry axis and causes no distortion of phase-velocity surfaces but results in rapid variations of qS-wave polarizations. To mitigate the artifacts due to the kiss singularity, we taper the polarization vector of two S-waves at the vicinity of the symmetry axis using the polar angle information.

A 3D numerical experiment demonstrates the decoupling of two S-wave modes. Figure 1 shows the synthetic vector elastic wavefield snapshots within a two-layer VTI model. The background parameters are $V_{\mathrm{P0}} = 3000\,\mathrm{m/s}$, $V_{\mathrm{S0}} = 2000\,\mathrm{m/s}$, $\rho = 2000\ \mathrm{g/cm^3}$, $\epsilon = 0.2$, $\delta = 0.1$, and $\gamma = 0.15$, and a mass density perturbation $\Delta\rho = 300\ \mathrm{g/cm^3}$ is added in the bottom to make an interface with dip angle of 135° strikes toward the y-axis. The grid size of the model is $201 \times 201 \times 201$ with a spatial increment of 10 m. To prevent the S-wave causing reflection, a pure qP-source (Wang et al., 2015b) is excited at the center of this model. Figure 2 shows the reflected qSV and qSH wavefields separated by equation 4. They respectively polarize in and perpendicular to the plane defined by the symmetry axis and polarization direction of the incident qP-wave. Of fundamental importance is that the qSH- and qSV-waves are not completely equivalent to qS1- and qS2-waves, respectively. As shown in Figure 3, the decomposed two S-waves own exactly the same amplitude compared with the original elastic wavefield. As shown in Figure 4, the qSV-wave can be converted from qS2 to qS1 mode at a certain oblique propagation angle (where the line singularity happens), whereas the qSH-wave can be converted from qS1 to qS2 mode likewise. In addition, the original elastic wavefield also can be decomposed into vector wavefield of each wave mode by equation 5.

For isotropic media, the polarization directions are independent of medium parameters, so the corresponding mode separation can be efficiently implemented as a stationary spatial filtering. In this case, equation 4 automatically reduces to the divergence operation for P-wave. For S-wave, however, the propagation velocity is constant no matter in which direction it polarizes. Therefore, the polarization of S-wave owns singularity at every point during the propagation (Tsvankin et al., 2001). To make the polarization-based

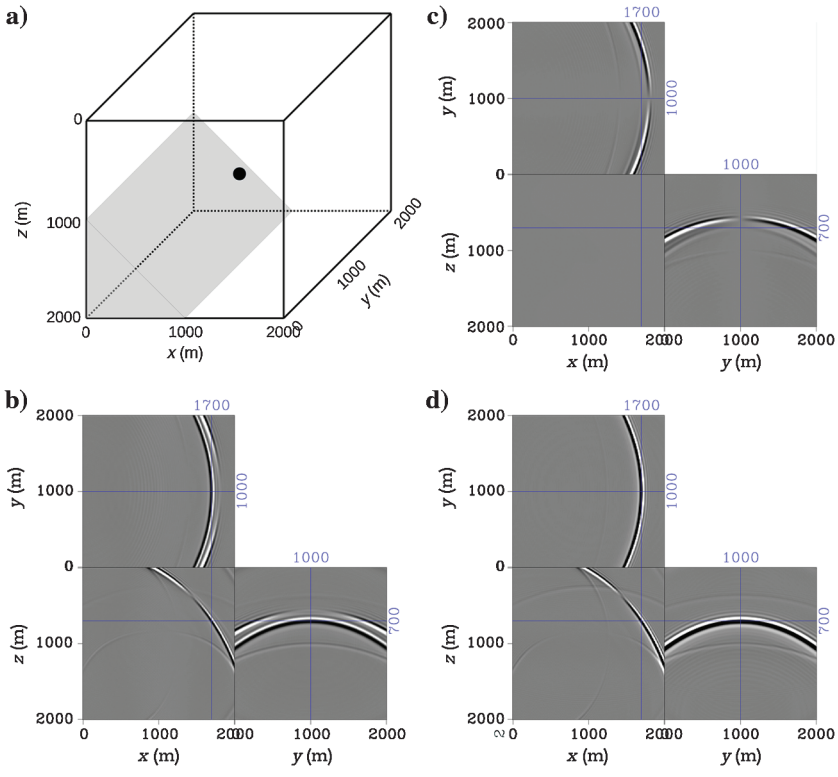

Figure 1. The 3D wavefield modeling in VTI media: (a) model geometry, the black dot indicates the source coordinate, panels (b-d) are x-, y-, z-component of vector original elastic wavefield at the time of 0.95 s, respectively. Despite the artifacts caused by imperfect PML, the reflected S-wave splits into two S-waves.

mode decoupling work for the S-waves when the medium changes from TI to isotropic, we have to artificially give a symmetry axis for the isotropic medium to define the polarization directions for qSV- and qSH-waves. In practice, most of the horizons in the subsurface are horizontally layered. Accordingly, we assume this "symmetry-axis" always vertical. In other words, the polarization vectors of qSV- and qSH-waves are defined based on the propagation direction of P-wave and the z-axis, namely,

$$\bar{\mathbf{a}}_{\mathrm{SH}} = D^{-1}(-\bar{k}_y, \bar{k}_x, 0), \quad \text{and} \quad \bar{\mathbf{a}}_{\mathrm{SV}} = D^{-1}(\bar{k}_x\bar{k}, \bar{k}_y\bar{k}_z, \bar{k}_z^2 - 1), \tag{7}$$

where $D = \sqrt{\bar{k}_x^2 + \bar{k}_y^2}$.

Efficient solution

For heterogeneous TI media, the polarization-based mode decoupling is prohibitively expensive because the operations become nonstationary filtering, which is locally determined by the material-dependent polarization directions. The computational complexity of the straightforward implementation is $O(N_x)^2$, where the N_x denotes the grid size of the model. To break this computational bottleneck, Cheng and Fomel (2014) rewrite equations 4 and 5 as mixed-domain Fourier integral operation (FIO) of the general form, respectively,

$$u_m(\mathbf{x}) = \int e^{i\mathbf{kx}} i\bar{\mathbf{a}}_m(\mathbf{x}, \mathbf{k}) \cdot \tilde{\mathbf{u}}(\mathbf{k}) \mathrm{d}\mathbf{k} \tag{8}$$

and

$$\mathbf{u}_m(\mathbf{x}) = \int e^{i\mathbf{kx}} \bar{\mathbf{a}}_m(\mathbf{x}, \mathbf{k})[\bar{\mathbf{a}}_m(\mathbf{x}, \mathbf{k}) \cdot \tilde{\mathbf{u}}(\mathbf{k})] \mathrm{d}\mathbf{k}, \tag{9}$$

where the integral kernel matrices are based on the medium parameters and the wave vector. By applying low-rank decomposition to these mixed-domain matrices, we can achieve very efficient mode separation and vector decomposition for ERTM application. The computational cost is based on the model size, the desired accuracy, and complexity of the kernel matrix of the FIOs (implicitly depending on the heterogeneity and anisotropy strength of the TI media). Mathematically, the computational complexity reduces to $O(NN_x \log N_x)$, where N represents the rank of decomposed mixed-domain matrix. Usually, the N is less than 10 (Cheng and Fomel, 2014).

Taking the previous 3D model as an example, it takes 55.2 s to simulate the elastic wavefield by using a 10th-order staggered-grid finite-difference (FD) algorithm (Virieux, 1986) with a single thread for one time step on average. As shown in Figure 5, it takes approximately 25.1 s to separate the simulated elastic waves into three (namely qP, qSV, and qSH) scalar wavefields, and approximately 50.7 s into three vector wavefields. The time cost for precalculation of matrix decomposition by the low-rank method (offline calculation) is not counted here. Similar with constructing time table in the ray-based migration method, once the offline calculation has been done, the results are available for every time step. Meanwhile, the dimension of the decomposed matrix is much smaller than the model size thus does not require too much I/O. During application of the imaging condition for ERTM, it is feasible to decouple the wave mode in every several time steps.

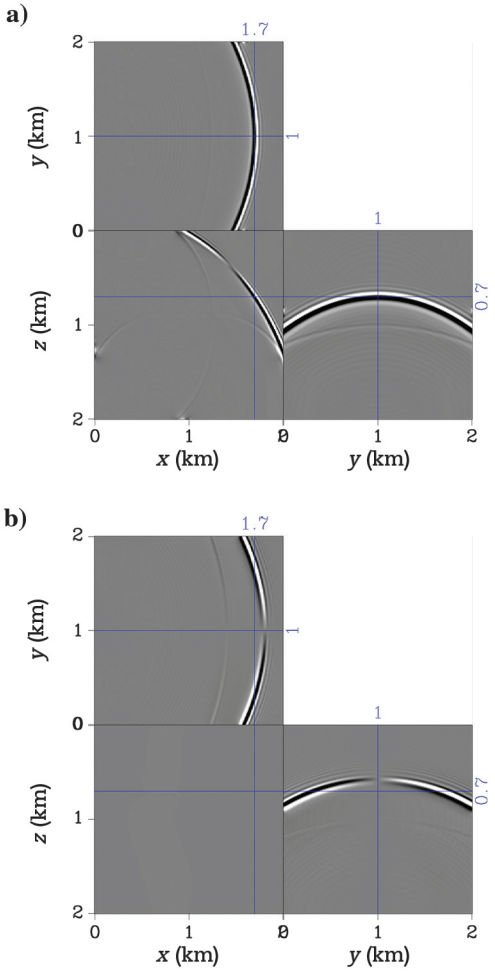

Figure 2. Separated scalar qS-waves: (a) qSV-wave and (b) qSH-wave. It is obvious that the two S-waves have different propagation velocity.

SCALAR IMAGING OF DECOUPLED WAVE MODES

The scalar imaging condition is based on the scalar wavefields of single wave mode. To our knowledge, most of the existing ERTM approaches apply imaging condition to the scalar (or scalarized) wavefields separated by the Helmholtz decomposition theory (equation 1) (Sun et al., 2006; Yan and Sava, 2008; Du et al., 2014). In the 2D case, the direction of the curl vector is perpendicular to the plane of the 2D model, so there is only one component for the separated S-wave. This is why many authors treat the 2D S-wave as a scalar field to produce the PS or SP image (Denli et al., 2008; Yan and Sava, 2008; Zhang and McMechan, 2011a). In 3D/3C, the separated S-wave by using the curl operation is a 3C vector, which means there is no single-signed scalar value to uniquely express it. This causes difficulty when we apply a crosscorrelation imaging condition to the two potential fields unless a scalarization is applied to the S-wavefield (Sun et al., 2006; Du et al., 2014) or a vectorization is applied to the P-wavefield (Duan and Sava, 2015). But it is cumbersome to appropriately scalarize or vectorize the potential and accurately assign its sign at every spatial point in complicated

elastic wavefields. Thus, the divergence and curl operations are not suitable to extend the imaging condition to obtain a 3D converted-wave image that is comparable with the PP image.

Scalar imaging condition

To extend the ERTM into anisotropic media, Zhang and McMechan (2011b) choose to apply an excitation imaging condition. However, the previous studies showed that the crosscorrelation imaging condition is considered stable and amplitude friendly (Chattopadhyay and McMechan, 2008; Costa et al., 2009). Thanks to the fast algorithm based on low-rank decomposition of the mixed-domain matrices in the FIOs for polarization-based mode decoupling, we achieve scalar imaging for TI media using

$$I_{mn}(\mathbf{x}) = \int_0^{t_{\max}} u_m^s(\mathbf{x}, t) u_n^r(\mathbf{x}, t) dt, \tag{10}$$

where u_m^s and u_n^r represent the single-mode source and receiver wavefields, respectively. For example, zero-lag crosscorrelating $u_{\mathrm{qP}}^s(\mathbf{x}, t)$ with $u_{\mathrm{qSV}}^r(\mathbf{x}, t)$ produces the image for PS-waves. A normalization factor representing source illumination can be added to the above imaging condition to improve the image quality (Mittet et al., 1995). Recall that this crosscorrelation imaging condition is different from those applied to the potential fields (Wapenaar et al., 1987; Yan and Sava, 2008).

Mapping zero-lag images into incident phase angles

To generate angle-domain CIGs, we should map and stack the zero-lag ERTM image into the local incident phase angle/azimuth bins at the image point. There are three normalized vectors associated with a local reflection orientation: the incident (phase) slowness vector in the source wavefield $\mathbf{p}_s$, the scattering (phase) slowness vector in the receiver wavefield $\mathbf{p}_r$, and the unit vector representing the direction normal to the geologic interface. Although it is possible to estimate the local angle attributes using the incident and scattering slowness vectors at the image point (Xu et al., 2011; Cheng et al., 2012), we tend to calculate them using the incident slowness vector and reflector normal because the receiver wavefield is more complicated than the source wavefield or the reflector shape. First, we apply the plane-wave destruction filter (Fomel, 2002) to the stacked PP image to calculate the normal direction of the reflectors. Then, we estimate the incident Poynting vector $\mathbf{w}$ at the time of maximum energy flow t_e using (Cerveny, 2005):

$$w_i(\mathbf{x}, t_e) = -\sigma_{ij}(\mathbf{x}, t_e) v_j(\mathbf{x}, t_e), \tag{11}$$

with

$$t_e(\mathbf{x}) = t | \max[E((\mathbf{x}), t)], \tag{12}$$

where σ_{ij} and v_j denote the stress and particle velocity, respectively. The mechanical energy E is calculated by

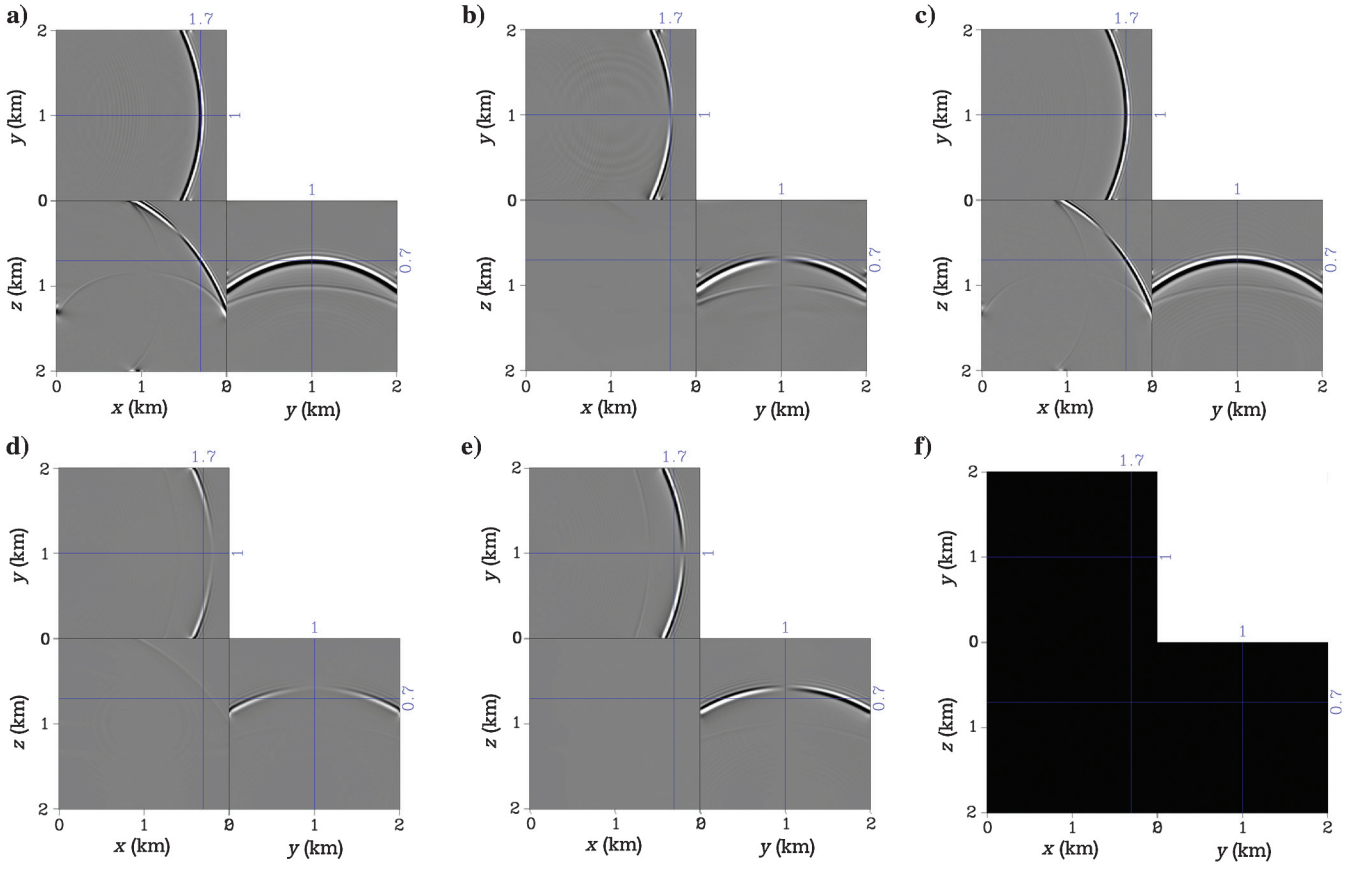

Figure 3. Decomposed vector qS-waves: (a) x-, (b) y-, and (c) z-component of qSV-wave and (d) x-, (e) y-, and (f) z-component of qSH-wave. Due to the qSH-wave being polarized in the horizontal plane in 3D VTI media, it has a null vertical component.

$$E(\mathbf{x},t)=\frac{1}{2}\rho v_i^2(\mathbf{x},t)+\frac{1}{2}\sigma_{ij}(\mathbf{x},t)\epsilon_{ij}(\mathbf{x},t), \qquad (13)$$

with the first term on the right side standing for the kinetic energy and the second standing for the potential energy of the source wavefield; ρ and ϵ_{ij} represent the mass volume density and strain fields, respectively. The Poynting vector is equivalent to the group direction, with $(\sin\alpha\cos\beta, \sin\alpha\sin\beta, \cos\alpha)=(w_x,w_y,w_z)/|\mathbf{w}|$ for the 3D case or $(\sin\alpha,\cos\alpha)=(w_x,w_z)/|\mathbf{w}|$ for the 2D case, where α and β are open angle from the z-axis and the azimuth angle of the group direction, respectively. Because reflection properties are governed by the phase angle (Thomsen, 1986; Tsvankin et al., 2001), an additional adjustment from the group to phase angle is needed for TI media. Then, we calculate the incident phase angle with respect to the normal direction of the reflector. Finally, we obtain the angle-domain CIGs by stacking the zero-lag ERTM image into the incident phase angle bins for all shots.

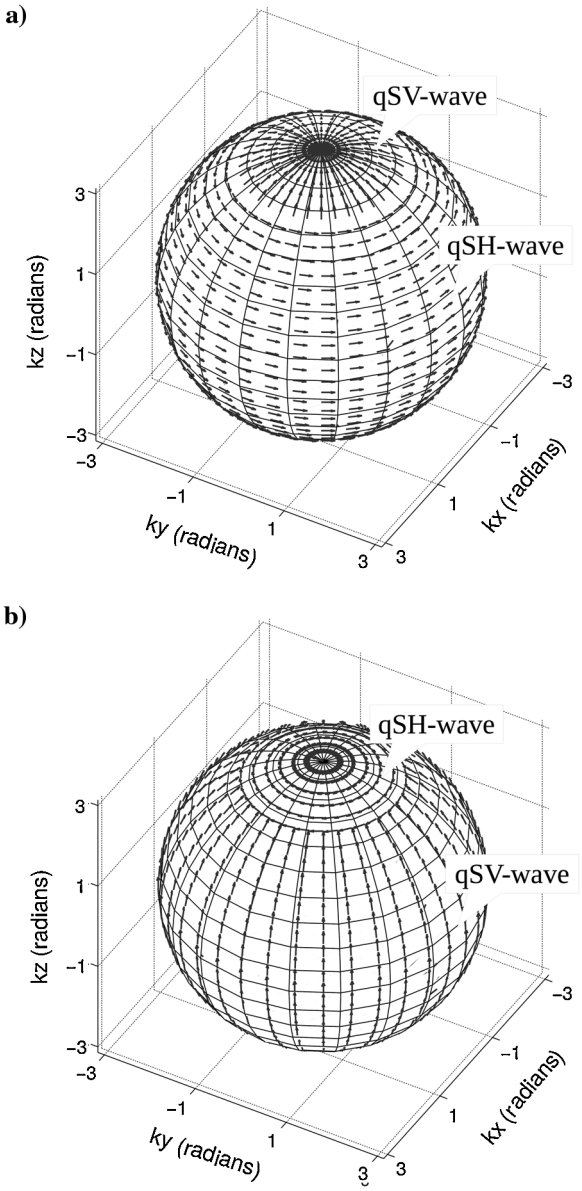

Figure 4. Polarization vectors of 3D qS-waves in the previously used VTI medium: (a) qS1- and (b) qS2-wave. Note that the qS1- and qS2-waves distinguished by phase velocity do not have continuous polarization and they can be designated as qSH- and qSV-waves, which have consistent polarization as a function of propagation direction. Modified from Figure 9 in Cheng and Kang (2016).

Polarity reversal in converted wave scalar imaging

Elastic wave polarization contains the geometric properties of particle motion, including trajectory shape and spatial orientation. Polarization of a separated body wave in a noise-free perfectly elastic medium is linear, and the motion has polarity (Winterstein, 1990). The change in wavelet polarity is a fundamental feature of converted waves due to the vector nature of the displacement field. Therefore, one difficulty when imaging the converted waves is the polarity change of the S-wave at a certain incident angle, which results in destructive contribution during stacking. It cannot be automatically addressed once the vector S-wave has been scalarized after mode separation or during application of the imaging condition. Many authors suggest preprocessing the S-wavefield with a reasonable sign (Balch and Erdemir, 1983; Denli et al., 2008; Du et al., 2014). In fact, the local angle-domain provides a natural domain to address this because the sign of a converted wave depends on the incident direction with respect to the interface normal (Rosales and Rickett, 2001; Lu et al., 2010). Therefore, we flip the sign of the converted-wave image at negative incident angles to correct the polarity reversal. For clarity, we demonstrate the workflow of angle-domain ERTM using cross-correlation imaging condition to the decoupled scalar wavefields in Figure 6.

VECTOR IMAGING OF DECOUPLED WAVE MODES

To take full advantage of the vector information (e.g., polarization and polarity) of the elastic wavefields, we propose a new imaging condition based on vector decomposition of the elastic wavefields for isotropic and TI media in this section.

Vector imaging condition

Vector decomposition decouples the elastic wavefields into vector fields of single wave mode, which owns the same polarization,

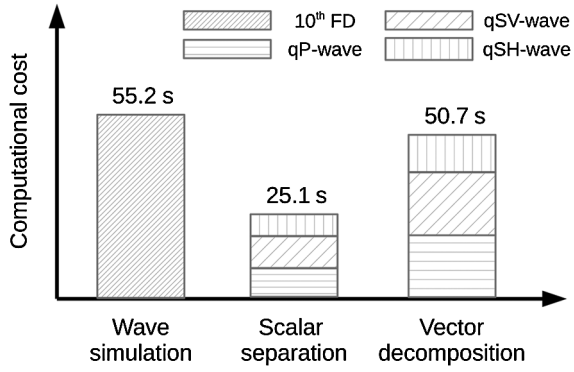

Figure 5. The computational cost of the polarization-based decoupling in a single time step of the 3D VTI model (in Figures 1–3). The low-rank decomposition approximate the mixed-domain matrix with relative single-precision of $1e^{-4}$. None of the parallel algorithms are used for accelerating computation.

polarity, amplitude, and phase of the counterpart in the original elastic wavefields. Following the investigation by Wang et al. (2015a), we propose a crosscorrelation imaging condition to the single-mode source and receiver wavefields in vector form:

$$I_{mn}(\mathbf{x}) = \frac{1}{\gamma}\int_0^{t_{\max}} [\mathbf{u}_m^s(\mathbf{x},t)\cdot\mathbf{u}_n^r(\mathbf{x},t)]dt, \quad (14)$$

with the scale factor γ defined by

$$\gamma = \int_0^{t_{\max}} [\mathbf{e}_m^s(\mathbf{x},t)\cdot\mathbf{e}_n^r(\mathbf{x},t)]dt, \quad (15)$$

using the unit polarization vectors of the source and receiver wavefields $\mathbf{e}_m^s$ and $\mathbf{e}_n^r$ to balance the migration amplitude.

The single-mode vector field separated from the source wavefields contains correct polarization information. Hence, we calculate the incident polarization direction at the time of maximum energy using the direction cosines as follows:

$$(\sin\theta\cos\varphi, \sin\theta\sin\varphi, \cos\theta) = (u_{sx}^m, u_{sy}^m, u_{sz}^m)/|\mathbf{u}_s^{(m)}| \quad (16)$$

for 3D or

$$(\sin\theta, \cos\theta) = (u_{sx}^m, u_{sz}^m)/|\mathbf{u}_s^{(\mathbf{m})}|, \quad (17)$$

for 2D, where θ and φ represent the open angle from the z-axis and azimuth angle of polarization direction. Then, we transform the incident polarization angles to phase angles using the relationship between them (Tsvankin et al., 2001). Finally, we map and stack the zero-lag ERTM image into the incident phase angle bins for all shots. To our interest, vector imaging condition, intrinsically exploiting polarity information, can give the correct sign of the converted-wave images. Therefore, correction of polarity reversal is excluded in the work flow of angle-domain ERTM using the crosscorrelation imaging condition for the decoupled vector wavefields (see Figure 7).

NUMERICAL EXAMPLES

We demonstrate the scalar and vector imaging approaches of ERTM with 2D and 3D synthetic data sets. The first two examples involve simple layered VTI models, and the third involves a complex VTI model. A 10th-order explicit staggered-grid FD algorithm is used to extrapolate the source and receiver wavefields. A perfectly matched layer (PML) absorbing boundary is used around the calculation area. We use the Laplacian filter (Mulder and Plessix, 2004) to suppress the low-wavenumber noise in the ERTM image. Regarding the receiver wavefields reconstruction, if only the data of particle velocity and dipole back-propagating sources are used, two types of wavefield artifacts will occur. First, all injected energy will upward and downward propagate unlike it truly comes from; second, any kind of events in recordings emit P and S energy simultaneously when injected for backward extrapolation (Yan and Sava, 2007). To mitigate the contamination from these artifacts, we combine the stress-velocity data and quadrupole-dipole back-propagating sources as a new top boundary condition for receiver wavefield reconstruction (Mittet, 1994; Ravasi and Curtis, 2013).

A two-layer 2D VTI model

A simple two-layer model is shown in Figure 8a with horizontal and dipping interfaces. The parameters are $V_{P0} = 2400$ m/s, $V_{S0} = 1400$ m/s, $\epsilon = 0.2$, and $\delta = 0.18$ in the first layer, and $V_{P0} = 3200$ m/s, $V_{S0} = 1800$ m/s, $\epsilon = 0.18$, and $\delta = 0.16$ in the second layer. A total of 101 common-shot gathers are synthesized for migration. Figure 8b and 8c shows the snapshots of x- and z-component of original vector elastic wavefields of the 51st shot located at $x = 500$ m and $z = 10$ m. With an exploding source, the

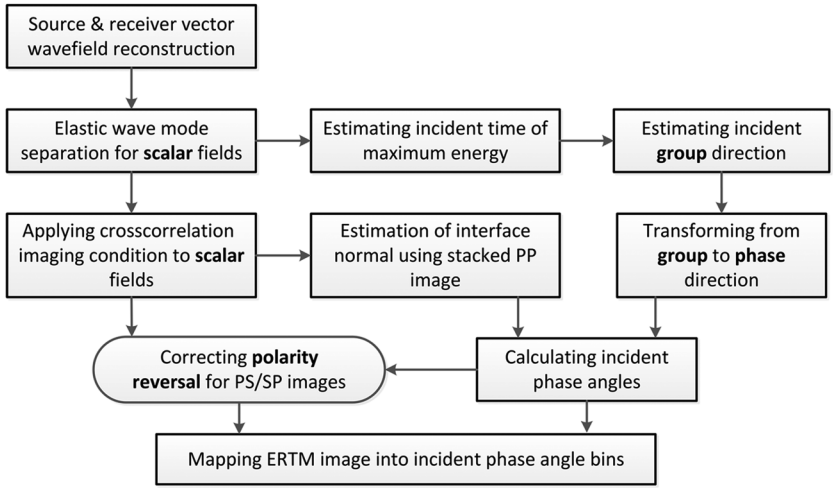

Figure 6. Workflow of angle-domain ERTM using crosscorrelation imaging condition with the decoupled scalar wavefields for TI media.

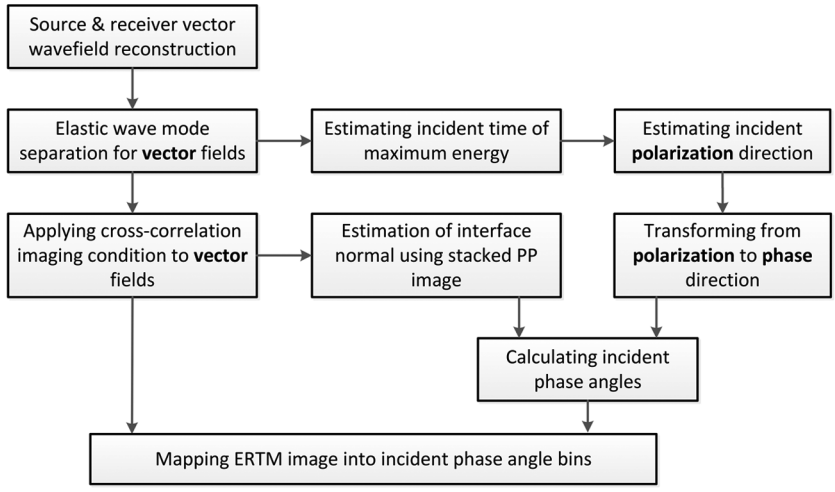

Figure 7. Workflow of angle-domain ERTM using crosscorrelation imaging condition with the decoupled vector wavefields for TI media.

source and receiver wavefields are mixed with qP- and qSV-wave modes. Consequently, the divergence and curl operations cannot achieve complete mode decoupling, whereas the polarization-based projection produces very clean single-mode scalar fields (see Figure 9). As shown in Figure 10, if polarization-based vector decomposition is applied, we achieve amplitude-preserved wave mode decoupling. On the single-shot ERTM images (Figure 11), migration artifacts related to the leaking mode are evident if the divergence and curl operations are used. Fortunately, the polarization-based mode separation and vector decomposition lead to very clean PP and PS images. Note that unlike the scalar imaging condition, the vector imaging condition produces PS image free of polarity reversal.

For mapping the zero-lag ERTM images into the incident angle domain, we have to transform the calculated group direction (using Poynting vector) or polarization direction (contained in the decomposed vector fields) to phase direction at the time of the maximum mechanical energy t_e. During the wavefield extrapolation, if the mechanical energy is larger than the previous time step on a certain spatial grid, we calculate and update the corresponding incident Poynting vector. Therefore, the storage of original elastic wavefield is not necessary. Due to the limitation of the cache memory, however, the decoupled wavefield of a single mode is stored into disk memory. As demonstrated in Figure 12, the transform from the group (or polarization) angle to phase angle is nontrivial because the maximum deviation is approximately 9° between group and phase directions and approximately 7° between polarization and phase directions for the incident qP-wave of the 51st shot.

As demonstrated in Figure 12b, the numerically estimated group and polarization angles from the extrapolated source wavefields match well with those calculated using the analytical relations between the group (or polarization) angle and the phase angle (Tsvankin et al., 2001).

Figure 12c shows that the transformed phase angles from the group (or polarization) angles are accurate, so can be used in angle-domain imaging. On the angle-domain CIGs stacked from the 101 shots zero-lag ERTM images, we observe migration artifacts

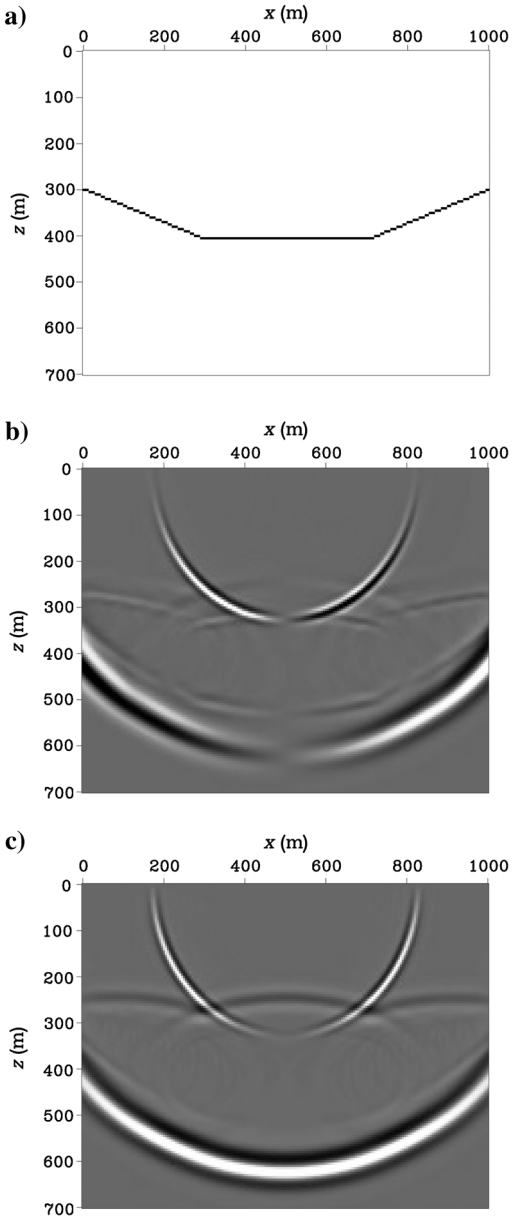

Figure 8. Snapshots of elastic wavefields from the source side in a two-layer VTI model: (a) Geometry of the model, (b) x-, and (c) z-component.

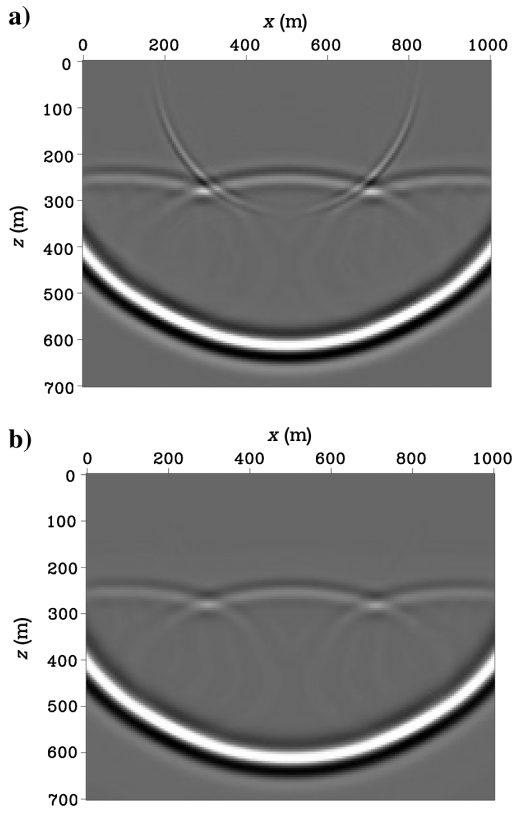

Figure 9. Separated scalar qP-wave in source wavefield by using (a) the divergence operation and (b) the polarization-based scalar projection.

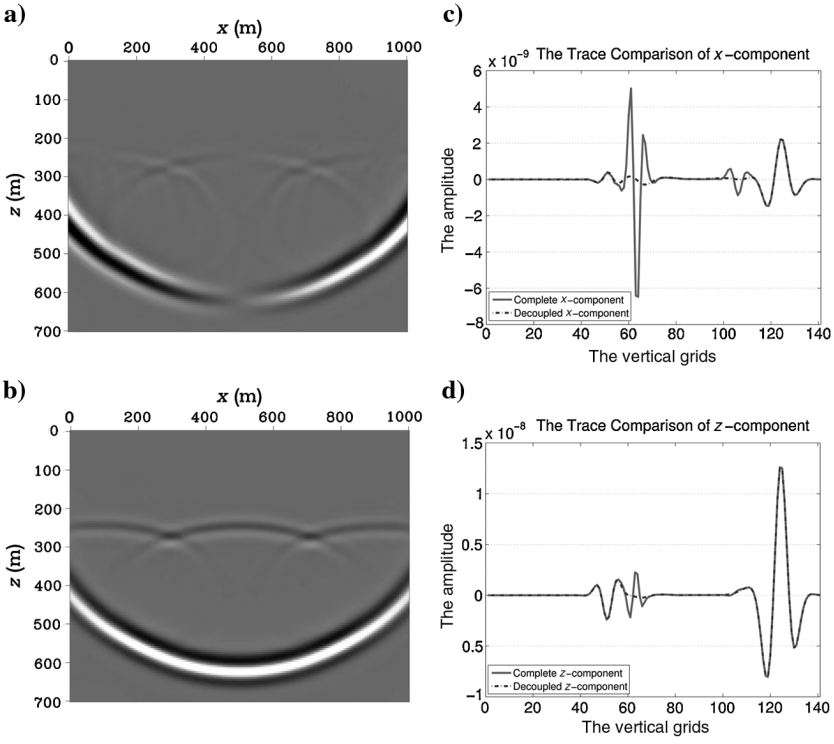

Figure 10. Decoupled vector qP-wave modes in the source wavefield using polarization-based vector decomposition: (a) x- and (b) z-component of qP-wave. A single trace extracted at $x = 600$ m for (c) x- and (d) z-component from the original and decoupled source wavefields. The orange solid lines indicate the total elastic wavefields (extracted from Figure 8b and 8c), and the black dash lines indicate the decoupled elastic wavefields.

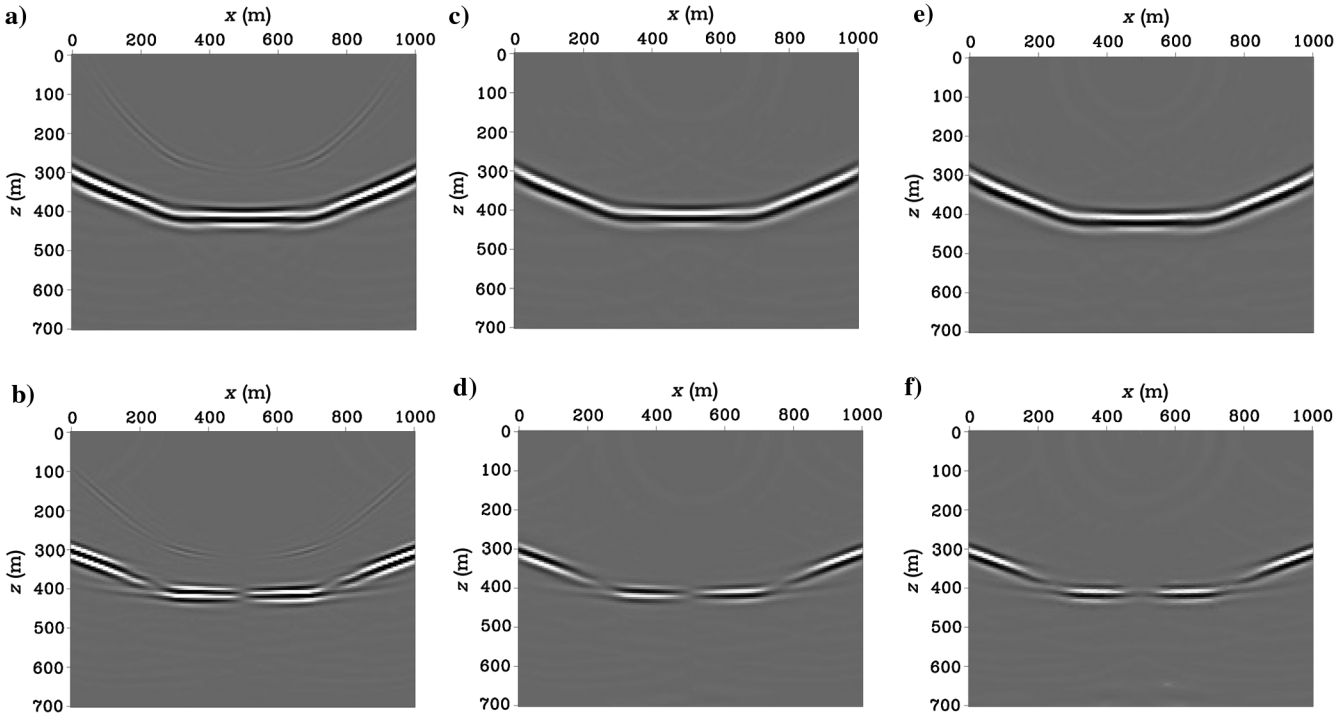

Figure 11. PP (top) and PS (bottom) ERTM images of the 51st shot respectively using scalar wavefields separated by the divergence and curl operators (left) and polarization-based scalar projection (middle), and vector wavefields separated by polarization-based vector decomposition (right). Note the migration artifacts due to mode-leaking in the shallow parts of left two pictures.

on PP and PS images due to mode leaking related to the divergence and curl operations (Figure 13a and 13d). The polarity reversal of PS images occurs within the scalar imaging result (Figure 13e). The angle-domain vector imaging produces very accurate and clean CIGs and automatically avoids polarity reversal for converted wave imaging. To obtain correctly stacked PS images, we apply the proposed approach to address polarity reversal in the angle-domain scalar imaging workflow. As observed by Lu et al. (2010), stacking of multiple sources can mitigate the migration artifacts from mode leaking with respect to the divergence and curl operations. For this simple model, the two workflows produce very similar stacked images, we only show the final PP and PS images using the vector imaging condition (see Figure 14).

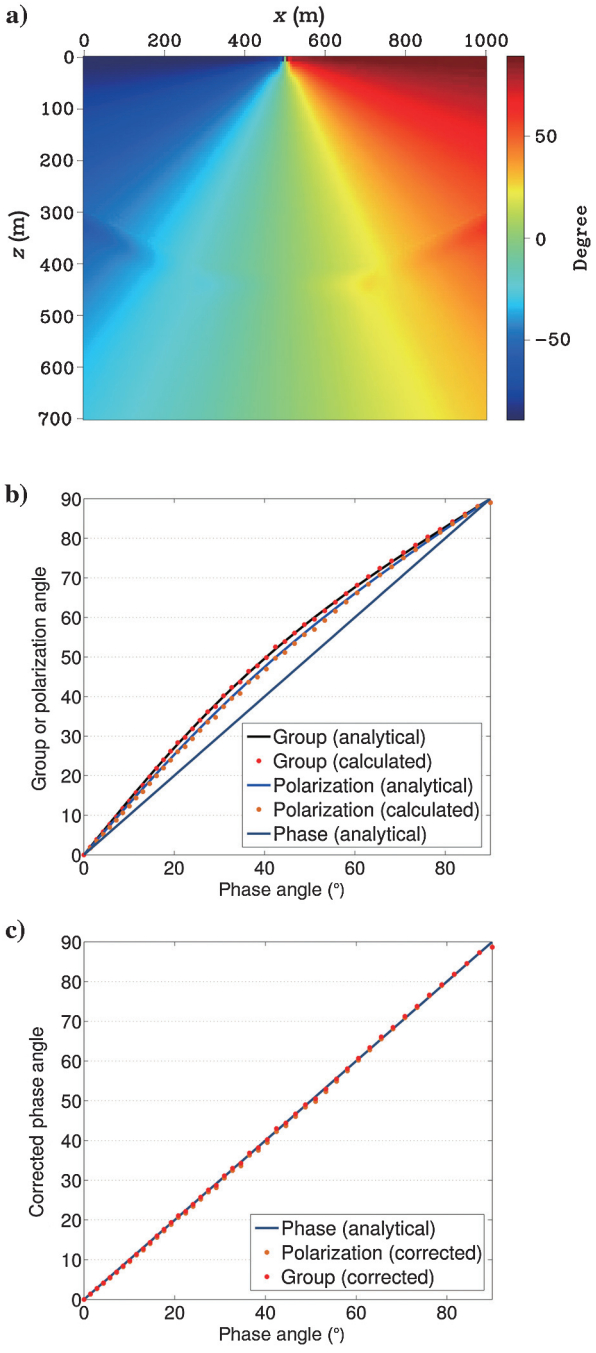

Figure 12. Transformation between group (or polarization) and phase angles for the incident qP-wave at the time of the maximum energy: (a) estimated phase angles; (b) angle comparison among group, polarization and phase angle (the dotted lines are estimated from the wavefield, and the solid lines are the analytical solution); and (c) transformation from group and polarization angle to phase angle.

A three-layer 3D VTI model

A three-layer VTI model with horizontal and dipping interfaces (Figure 15a) is used to demonstrate the proposed methods in 3D case. The first layer is a homogeneous VTI media with $V_{P0} = 2000$ m/s, $V_{S0} = 1328$ m/s, $\epsilon = 0.05$, $\delta = 0.03$, and $\gamma = 0.02$. The second is a homogeneous and isotropic medium, which has the parameters $V_P = 2300$ m/s and $V_S = 1628$ m/s. The third is also a homogeneous VTI medium, which has the parameters $V_P = 2600$ m/s, $V_S = 1928$ m/s, $\epsilon = 0.10$, $\delta = 0.06$, and $\gamma = 0.04$. On the top surface, we trigger nine exploding sources, which are symmetrically distributed like a 3×3 array around the center with an increment of 50 m. A Ricker wavelet with peak frequency is 15 Hz is chosen as the source function. Despite the artifacts resulting from the aperture limitation, the scalar and vector imaging algorithms produce comparable PP images (Figure 15b and 15e). For the PS image, the vector imaging algorithm uses the polarity information and automatically avoids the polarity reversal.

A complex 2D VTI model

To illustrate the proposed methods in complex media, we modify the Marmousi-2 model (Martin et al., 2006) to create a heterogeneous VTI model (Figure 16). We take the original P-wave velocity as the vertical qP-wave velocity and generate the vertical qSV-wave velocity using a scaling: $V_{P0}/V_{S0} = 1.7$. The two Thomson parameters increase linearly in depth with $\varepsilon \in [0, 0.13]$ and $\delta \in [0, 0.11]$, respectively. A total of 300 shots are simulated on the surface from $x = 250$ to 9250 m with a shot spacing of 30 m. As shown in Figures 17 and 18, the angle-domain scalar imaging based on polarization-based mode separation produces very good PP image and flatten angle-domain CIGs within -45° to 45°. But the polarity reversal shown on the CIGs leads to destructive interference during stacking of PS images from multiple sources. Fortunately, the proposed correction of polarity reversal in the local angle-domain greatly improves the final PS images (see Figure 17b). Moreover, high-quality ERTM images and angle-domain CIGs are obtained by using the vector imaging condition, which is directly applied to the decoupled source and receiver wavefields with polarization-based vector decomposition (Figures 19 and 20). This complex example further proves that the vector imaging condition automatically avoids the issue of polarity reversal.

DISCUSSION

Wave mode decoupling is a prerequisite for elastic imaging of multicomponent seismic data to produce physically interpretable images. However, the polarization-based scalar mode separation lose the polarity information because it only produces the scalar P- and S-wavefields. If the scalar imaging is used, polarity reversal

of converted-wave image will occur and the corresponding correction is indispensable. The correction amounts to a spatial operation depending on the incident angle, the interface normal, or energy flux direction at every image point (Du et al., 2012, 2014; Duan and Sava, 2015). Vector decomposition relies on more computation cost compared with scalar separation, but achieves accurate wave mode decoupling, and thus preserves the polarity information for each mode. Therefore, the converted-wave images produced by the vector imaging are immune to polarity reversal. If a S-wave source is triggered, based on the orthogonality among three wave modes and the direction of symmetry axis, the polarization direction of qP-wave also can be determined from the decoupled either qSV- or qSH-wavefields. Then, it can be transformed into incident phase direction as we discussed above. Meanwhile, the potential-based 3D ERTM method (Du et al., 2014; Duan and Sava, 2015) can be easily extended to TI media if the low-rank approximate solution of equation 3 is used.

To our knowledge, the term "vector imaging" is first named by Xie and Wu (2005) in their paper that describes a prestack depth migration approach using the one-way elastic wave propagator. During imaging, they first project the single-mode downgoing and upgoing vector wavefields onto their local polarization directions and then apply the crosscorrelation imaging condition to the resulted (namely scalarized) wavefields. They estimate the unit polarization vectors at the image point from the frequency-space-domain wavefields, although this is not straightforward (as they pointed out). In addition, wavefield extrapolation and mode coupling (to construct converted waves) are only designed for isotropic media in the framework of one-way wave propagation, and P/S separation of the multicomponent seismogram is needed before depth extrapolation of the wavefields. Alternatively, Zhang and McMechan (2011a) develop a direct vector-field method to obtain angle-domain CIGs from isotropic acoustic and elastic RTM. However, this approach needs extension for 3D anisotropic media because it does not distinguish polarization and phase directions in estimating the incident phase angle.

For isotropic and TI media, polarization-based projection decouples the elastic wavefields into three wave modes using their polarization orthogonality. It is easy to separate the compressional mode because it has well-behaved polarization properties. Decoupling the

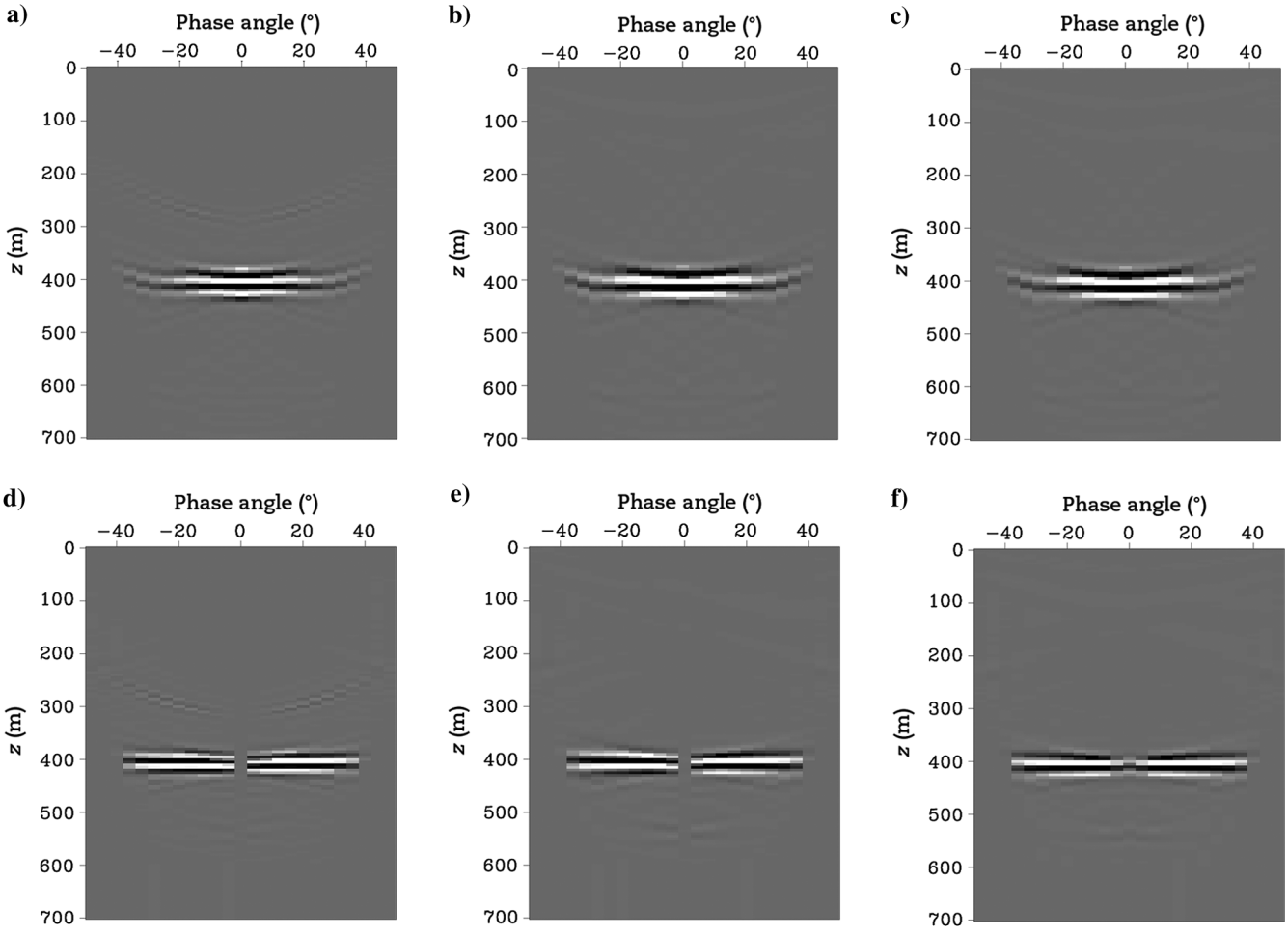

Figure 13. Angle-domain CIGs of reflected PP- (top) and PS-wave (bottom) at the location of $x = 500$ m: scalar imaging condition based on the Helmholtz decomposition (right) and polarization-based mode separation (middle), and vector imaging condition based on polarization-based vector decomposition (right).

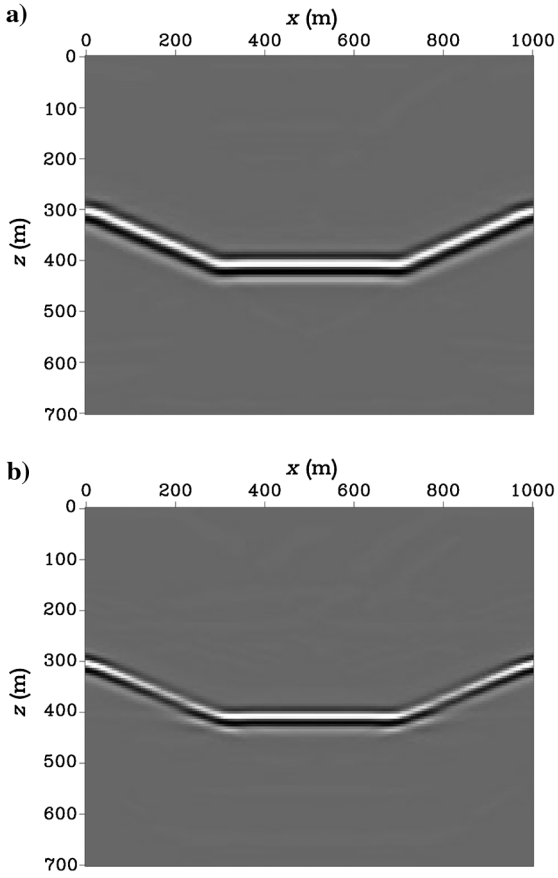

Figure 14. Final migrated PP (a) and PS (b) results of all 101 shots.

two shear modes in the 3D case, however, involves complexity on conceptual and methodological aspects. For instance, we designate the two qS-waves in a TI medium as qSV and qSH modes, which have consistent polarization as a function of propagation direction except at the kiss singularity. The polarization direction of the qSH mode is defined perpendicular to the plane determined by the symmetry axis and qP-wave polarization direction, and then the polarization direction of the qSV mode is determined through the polarization directions of qP and qSH modes, on the base of the qP-qSV-qSH polarization orthogonality. For isotropic media, however, people prefer to designate 3D S-wave as SV and SH modes. The SV-wave coupled with P-wave polarizes in the incident plane (instead of the symmetry-axis plane as in TI media), whereas the

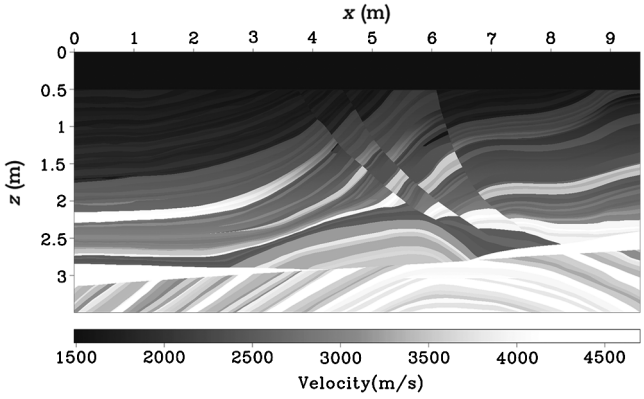

Figure 16. Vertical qP-wave velocity of a modified Marmousi-2 model.

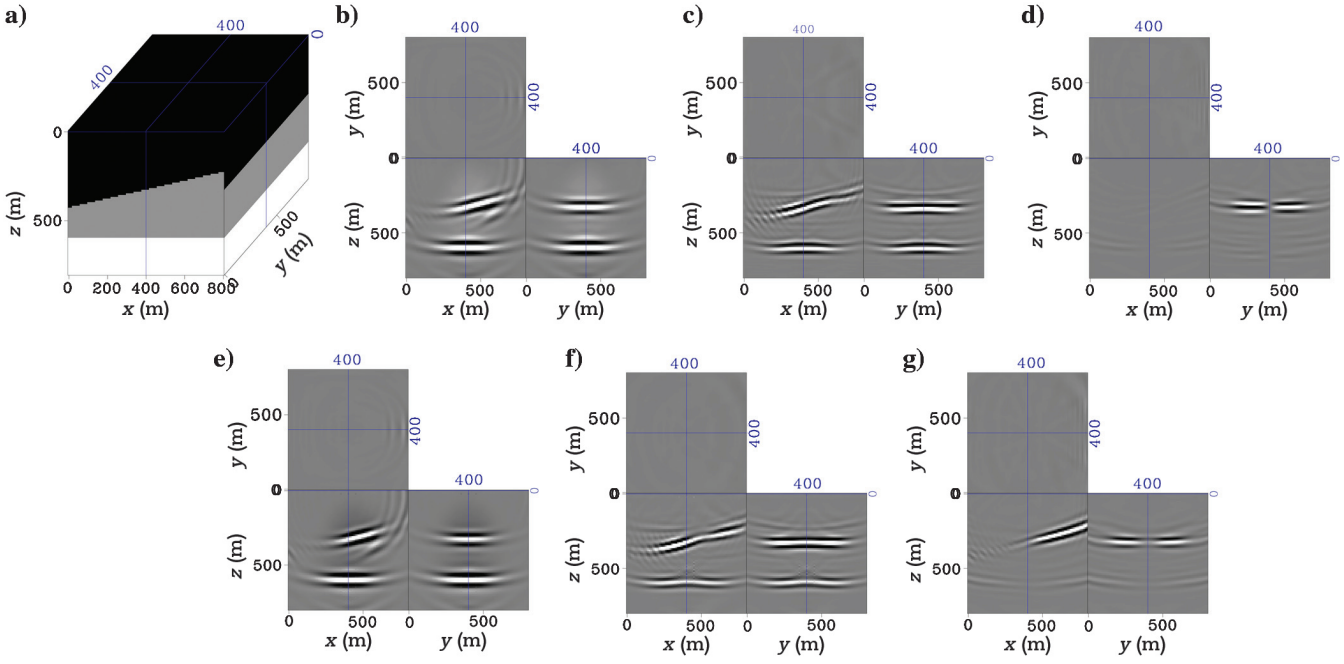

Figure 15. The ERTM experiment on a 3D VTI model with horizontal and dipping interfaces: (a) model geometry; (b) qP-qP, (c) qP-qSV, and (d) qP-qSH images using scalar imaging condition; (e) qP-qP, (f) qP-qSV, and (g) qP-qSH images using vector imaging condition. Only nine synthetic common-shot records are used for migration.

SH-wave polarizes orthogonally to this plane. Note that the incident plane is determined by the incident wave vector and the local interface normal. To make the polarization-based projection work when the medium changes from TI to isotropic, we have assumed that the isotropic medium has a hypothetical "symmetry axis" in the vertical direction. Physically, SH-wave is automatically decoupled from qP- and qSV-waves. In this paper, however, qSV-waves may be numerically decomposed into a qSV and a qSH component because the normal of local interface is not considered during the wave mode decoupling. For the qSV-wave reflected or converted from an interface, its decomposed qSH component is nonnull, unless the normal of the local interface is parallel with the symmetry axis. Generally, the decomposed qSV and qSH components have a contribution to qS-wave imaging. For TI media, investigation and integration of these two S-wave images may provide new opportunity for seismic imaging and medium parameter estimation because the polarization properties of the qSV and qSH modes are material dependent.

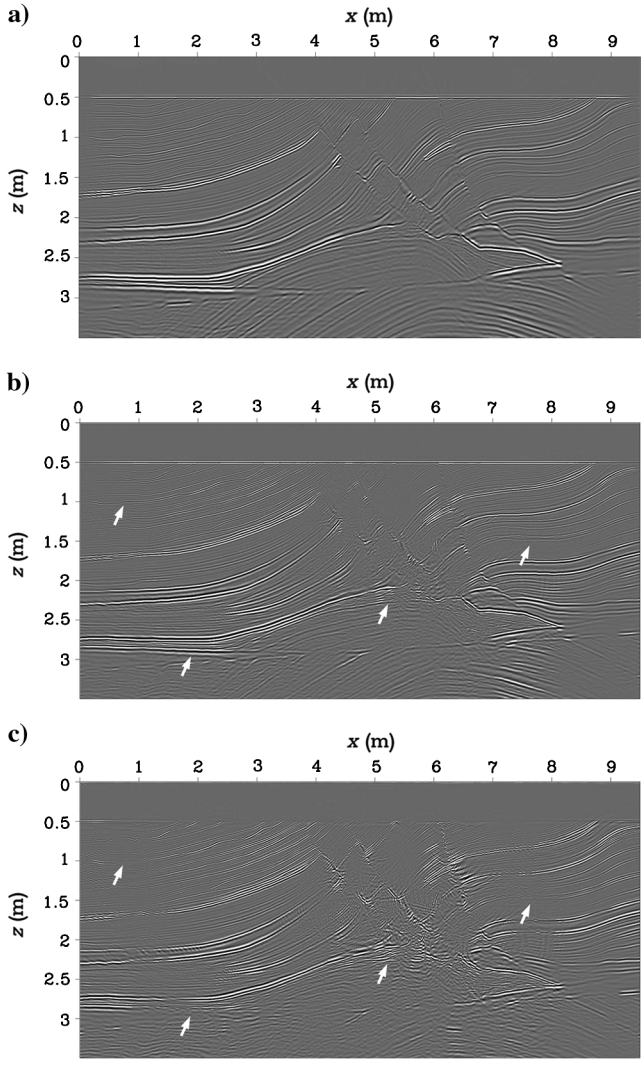

Figure 17. Final migrated results using the scalar imaging condition based on polarization-based mode separation: (a) PP image and PS images (b) with and (c) without correction of polarity reversal. White arrows indicate the improvements after correcting polarity reversal.

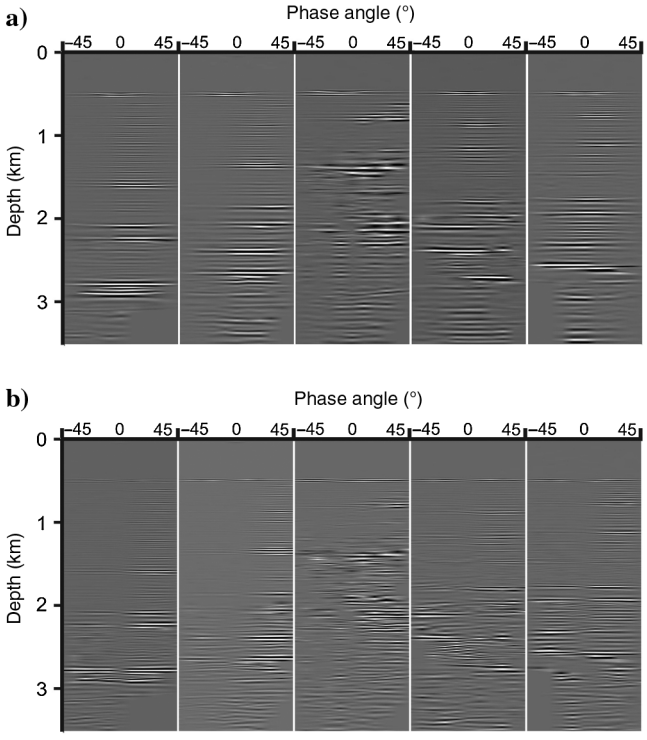

Figure 18. Angle-domain CIGs at $x = 2, 3, 5, 7$, and 8 km using the scalar imaging condition based on polarization-based mode separation: (a) PP and (b) PS CIGs (the polarity has not been corrected).

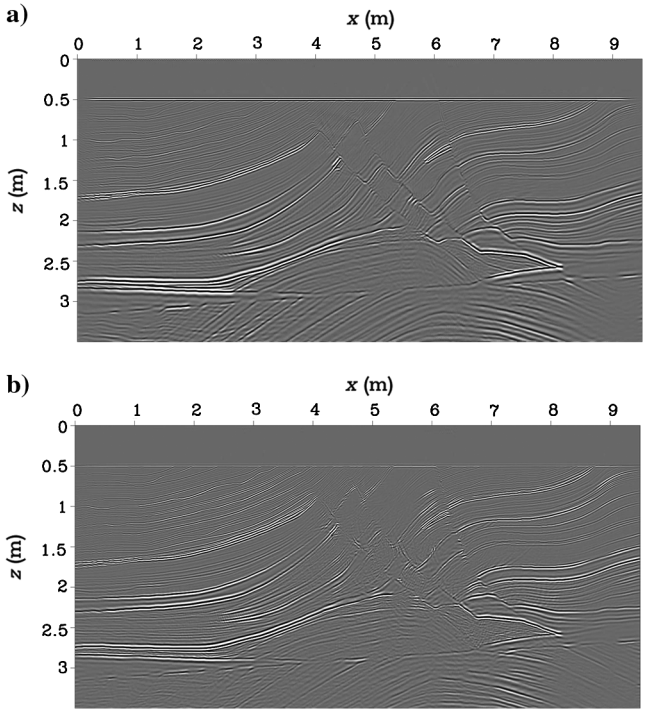

Figure 19. Final migrated results using the vector imaging condition based on polarization-based vector decomposition: (a) PP and (b) PS images.

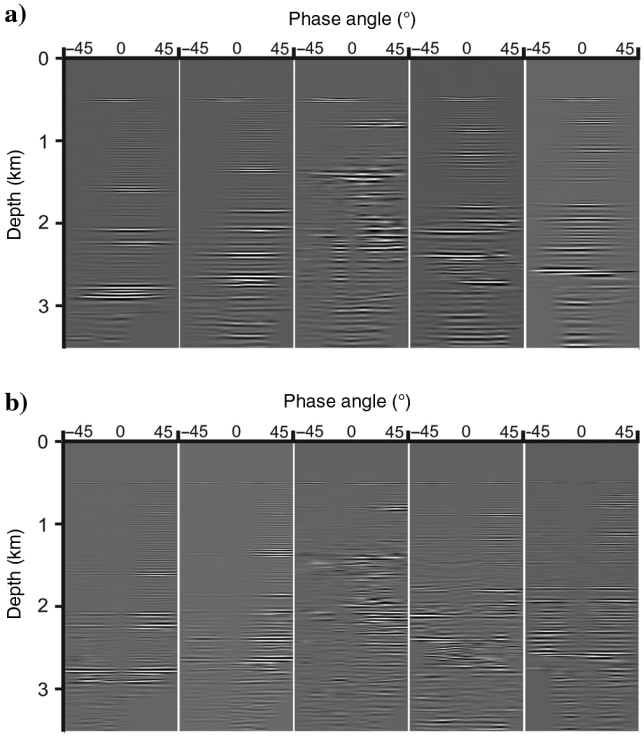

Figure 20. Angle-domain CIGs at $x = 2, 3, 5, 7$, and 8 km using the vector imaging condition based on polarization-based vector decomposition: (a) PP and (b) PS CIGs.

CONCLUSIONS

For heterogeneous isotropic and TI media, we have proposed new scalar and vector imaging conditions for 2D/3D ERTM. To obtain physically interpretable images for PP or PS reflections, polarization-based mode separation or vector decomposition is applied to the extrapolated elastic wavefields to provide single-mode scalar or vector wavefields. To map the zero-lag ERTM images into angle domain, the local phase directions of the incident qP-waves and the interface normals are used to calculate the local incident phase angle at every image point. For scalar imaging, the incident phase angle is transformed from the group angle (indicated by the Poynting vector), which is estimated from the extrapolated stress and velocity fields at the maximum energy time. And the local incident angle is directly used to correct the polarity reversals of the PS images. For vector imaging, the incident phase angles are transformed from the polarization angle, which is originally contained in the decoupled vector fields. Because vector decomposition provides high-fidelity single-mode wavefields, the resulting vector imaging condition produces more accurate migration, of which the converted wave images are immune to the polarity reversals.

For isotropic media, the two S-waves are inseparable during the wave propagation. We assume the "symmetry-axis" is vertical so that the algorithm can be generally used. Accordingly, these ERTM algorithms become relatively easy because it takes nearly negligible computational time for mode decoupling and there is no need to distinguish group, phase, and polarization directions for angular attribute calculation. For TI media, thanks to the fast algorithms for mode decoupling, we separate wave modes very efficiently and thus the crosscorrelation imaging condition can be used to achieve accurate imaging. The examples have demonstrated the validity and performance of the two approaches. Although the mode decoupling algorithm helps us to estimate the local angular attributes very efficiently, it is still challenging to calculated the local group, phase, and polarization directions of the complicated wavefields. We will continue to improve this step for angle-domain ERTM in the future work.

ACKNOWLEDGMENTS

This work is supported by the National Natural Science Foundation of China (grant no. 41474099), Shanghai Natural Science Foundation (grant no. 14ZR1442900), and National Science and Technology Major Program (grant no. ZX05027001-008). We are grateful to associate editor Faqi Liu and three other anonymous reviewers for their valuable comments. Chenlong Wang appreciates the ROSE Consortium for providing the computational and working environment when he studied at NTNU for one year supported by the China Scholarship Council (grant no. 201406260132). He would like to thank B. Ursin, W. Weibull, M. Ravasi, T. F. Wang, and Q. Hao for their helpful discussions. We appreciate the support of the Madagascar software package.

APPENDIX A

POLARIZATION VECTORS IN TI MEDIA

For TI media, the P-wave and the two S-waves do not polarize parallel or perpendicular to the wave vector. Generally, we obtain the polarization vectors $\mathbf{a}_m$ by solving the material-dependent Christoffel equation (Aki and Richards, 2002),

$$[\mathbf{G} - \rho V^2 \mathbf{I}]\mathbf{a}_m = 0, \tag{A-1}$$

where $m = \{\text{qP}, \text{qS1}, \text{qS2}\}$, $\mathbf{G}$ is the Christoffel matrix $G_{ij} = c_{ijkl}k_j k_l$, where c_{ijkl} is the stiffness tensor, and k_j and k_l are the normalized wave vector components in the j and l directions, $i, j, k, l = 1,2,3$. The parameter V corresponds to the eigenvalue of the matrix $\mathbf{G}$ and represents the phase velocity of a given wave mode. This equation allows us to compute the polarization vectors $\mathbf{a}_m$ (the eigenvectors of the matrix), especially $\mathbf{a}_\text{P}$ for the well-behaved qP-wave. As demonstrated by Winterstein (1990) and Zhang and McMechan (2010), the qS1 and qS2 distinguished by phase velocities do not always give consistent polarizations (the line singularity), Therefore, Zhang and McMechan (2011a) designate the qS-wave as qSV and qSH modes, which always have consistent polarizations except at the shear singularity along the symmetry axis (Crampin and Yedlin, 1981). This shear singularity is the so-called kiss singularity, due to the two S-waves having the same phase velocity along the symmetry axis. Accordingly, qSH-waves polarize perpendicular to the symmetry plane (polarizes in isotropy plane) and qSV-waves polarize in the symmetry planes. Based on this qP-qSV-qSH-polarization orthogonality (Figure A-1) and the calculated $\mathbf{a}_\text{P}$, the corresponding polarization vectors of two S-waves can be obtained in the wavenumber domain (Yan and Sava, 2012), yielding

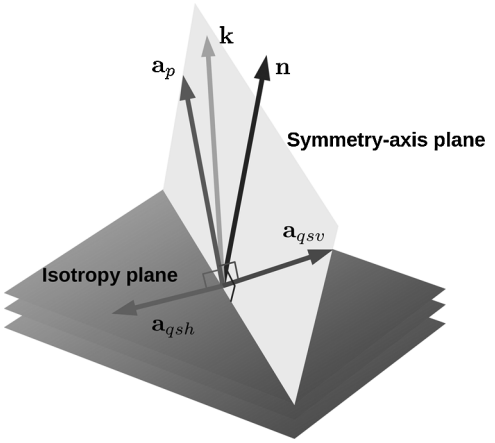

Figure A-1. Schematic demonstration of elastic wave mode polarization in 3D TI media. The three gray layers represent the isotropy plane; **n** is the symmetry axis; **k** refers to the propagation direction of the plane wave; and $\mathbf{a}_{\mathrm{P}}, \mathbf{a}_{\mathrm{qSV}}, \mathbf{a}_{\mathrm{qSH}}$, denote the qP-, qSV-, and qSH-wave mode polarization direction, respectively (Yan and Sava, 2012).

$$\mathbf{a}_{\mathrm{qSH}} = \mathbf{n} \times \mathbf{a}_{\mathrm{P}} \quad \text{and} \quad \mathbf{a}_{\mathrm{qSV}} = \mathbf{a}_{\mathrm{P}} \times \mathbf{a}_{\mathrm{qSH}}, \tag{A-2}$$

where **n** is a unit vector indicating the direction of symmetry axis.

REFERENCES

Aki, K., and P. G. Richards, 2002, Quantitative seismology: Theory and methods: University Science Books.

Balch, A. H., and C. Erdemir, 1983, Sign-change correction for prestack migration of P-S converted wave reflection: Geophysics, **48**, 1514–1524, doi: 10.1190/1.1441434.

Biondi, B., and W. Symes, 2004, Angle-domain common-image gathers for migration velocity analysis by wavefield-continuation imaging: Geophysics, **69**, 1283–1298, doi: 10.1190/1.1801945.

Cerveny, V., 2005, Seismic ray theory: Cambridge University Press.

Chang, W.-F., and G. A. McMechan, 1986, Reverse-time migration of offset vertical seismic profiling data using the excitation-time imaging condition: Geophysics, **51**, 67–84, doi: 10.1190/1.1442041.

Chattopadhyay, S., and G. A. McMechan, 2008, Imaging conditions for prestack reverse-time migration: Geophysics, **73**, no. 3, S81–S89, doi: 10.1190/1.2903822.

Cheng, J., and S. Fomel, 2014, Fast algorithms for elastic-wave-mode separation and vector decomposition using low-rank approximation for anisotropic media: Geophysics, **79**, no. 4, C97–C110, doi: 10.1190/geo2014-0032.1.

Cheng, J., and W. Kang, 2016, Simulating propagation of separated wave modes in general anisotropic media, Part II: qS-wave propagators: Geophysics, **81**, no. 4, C39–C52, doi: 10.1190/geo2015-0253.1.

Cheng, J., T. Wang, C. Wang, and J. Geng, 2012, Azimuth-preserved local angle-domain prestack time migration in isotropic, vertical transversely isotropic and azimuthally anisotropic media: Geophysics, **77**, no. 2, S51–S64, doi: 10.1190/geo2011-0295.1.

Claerbout, J. F., 1985, Imaging the earth's interior: Blackwell Scientific Publications Inc.

Costa, J., F. Silva Neto, M. Alcantara, J. Schleicher, and A. Novais, 2009, Obliquity-correction imaging condition for reverse time migration: Geophysics, **74**, no. 3, S57–S66, doi: 10.1190/1.3110589.

Crampin, S., 1991, Effective of point singularities on shear-wave propagation in sedimentary basins: Geophysical Journal International, **107**, 531–543, doi: 10.1111/j.1365-246X.1991.tb01413.x.

Crampin, S., and M. Yedlin, 1981, Shear-wave singularities of wave propagation in anisotropic media: Journal of Geophysics, **49**, 43–46.

Dellinger, J., and J. Etgen, 1990, Wave-field separation in two-dimensional anisotropic media: Geophysics, **55**, 914–919, doi: 10.1190/1.1442906.

Denli, H., L. Huang, and R. Zhou, 2008, A high-resolution vector-imaging condition for elastic reverse-time migration: 70th Annual International Conference and Exhibition, EAGE, Extended Abstracts, 1712–1716.

Dickens, T., and G. Winbow, 2011, RTM angle gathers using Poynting vectors: 81st Annual International Meeting, SEG, Expanded Abstracts, 3109–3113.

Du, Q., X. Gong, M. Zhang, Y. Zhu, and G. Fang, 2014, 3D PS-wave imaging with elastic reverse-time migration: Geophysics, **79**, no. 5, S173–S184, doi: 10.1190/geo2013-0253.1.

Du, Q., Y. Zhu, and J. Ba, 2012, Polarity reversal correction for elastic reverse time migration: Geophysics, **77**, no. 2, S31–S41, doi: 10.1190/geo2011-0348.1.

Duan, Y., and P. Sava, 2015, Scalar imaging condition for elastic reverse-time migration: Geophysics, **80**, no. 4, S127–S136, doi: 10.1190/geo2014-0453.1.

Fomel, S., 2002, Applications of plane-wave destruction filters: Geophysics, **67**, 1946–1960, doi: 10.1190/1.1527095.

Gray, S., J. Etgen, J. Dellinger, and D. Whitmore, 2001, Seismic migration problems and solutions: Geophysics, **66**, 1622–1640, doi: 10.1190/1.1487107.

Kuo, J., and T. Dai, 1984, Kirchhoff elastic wave migration for the case of noncoincident source and receiver: Geophysics, **49**, 1223–1238, doi: 10.1190/1.1441751.

Lu, R., J. Yan, P. Traynin, J. E. Anderson, and T. Dickens, 2010, Elastic RTM: Anisotropic wave-mode separation and converted-wave polarization correction: 80th Annual International Meeting, SEG, Expanded Abstracts, 3171–3175.

Ma, D. T., and G. M. Zhu, 2003, P- and S-wave separated elastic wave equation numerical modeling (in Chinese): Oil Geophysical Prospecting, **38**, 482–486.

Martin, G. S., R. Wiley, and K. J. Marfurt, 2006, Marmousi2: An elastic upgrade for Marmousi: The Leading Edge, **25**, 156–166, doi: 10.1190/1.2172306.

McGarry, R., and Y. Qin, 2013, Direction vector based angle gathers from anisotropic elastic RTM: 83rd Annual International Meeting, SEG, Expanded Abstracts, 3820–3824.

Mittet, R., 1994, Implementation of the Kirchhoff integral for elastic waves in staggered grid modeling schemes: Geophysics, **59**, 1894–1901, doi: 10.1190/1.1443576.

Mittet, R., R. Sollie, and K. Hokstad, 1995, Prestack depth migration with compensation for absorption and dispersion: Geophysics, **60**, 1485–1494, doi: 10.1190/1.1443882.

Mulder, W. A., and R.-E. Plessix, 2004, A comparison between one-way and two-way wave-equation migration: Geophysics, **69**, 1491–1504, doi: 10.1190/1.1836822.

Ravasi, M., and A. Curtis, 2013, Nonlinear scattering based imaging in elastic media: Theory, theorems, and imaging conditions: Geophysics, **78**, no. 3, S137–S155, doi: 10.1190/geo2012-0286.1.

Rosales, D., and J. Rickett, 2001, PS wave polarity reversal in angle domain common-image gathers: 71st Annual International Meeting, SEG, Expanded Abstracts, 1843–1846.

Sava, P., and S. Fomel, 2006, Time-shift imaging condition in seismic migration: Geophysics, **71**, no. 6, S209–S217, doi: 10.1190/1.2338824.

Stewart, R., J. Gaiser, R. Brown, and D. Lawton, 2002, Converted wave seismic exploration: Methods: Geophysics, **67**, 1348–1363, doi: 10.1190/1.1512781.

Sun, R., G. A. McMechan, C.-S. Lee, J. Chow, and C.-H. Chen, 2006, Prestack scalar reverse-time depth migration of 3D elastic seismic data: Geophysics, **71**, no. 5, S199–S207, doi: 10.1190/1.2227519.

Thomsen, L., 1986, Weak elastic anisotropy: Geophysics, **51**, 1954–1966, doi: 10.1190/1.1442051.

Tsvankin, I., K. Helbig, and S. Treitel, 2001, Seismic signatures and analysis of reflection data in anisotropic media: Pergamon.

Virieux, J., 1986, P-SV wave propagation in heterogeneous media: Velocity-stress finite-difference method: Geophysics, **51**, 889–901, doi: 10.1190/1.1442147.

Vyas, M., X. Du, E. Mobley, and R. Fletcher, 2011, Methods for computing angle gathers using RTM: 73rd Annual International Conference and Exhibition Incorporating SPE EUROPE, EAGE, Extended Abstracts, 1570–1574.

Wang, C., J. Cheng, and B. Arntsen, 2015a, Imaging condition for converted waves based on decoupled elastic wave modes: 85th Annual International Meeting, SEG, Expanded Abstracts, 4385–4390.

Wang, C., J. Cheng, and B. Arntsen, 2015b, Numerical pure wave source implementation and its application to elastic reverse time migration in anisotropic media: 77th Annual International Conference and Exhibition, EAGE, Extended Abstracts, 1028–1032.

Wang, C., J. Cheng, and T. Wang, 2014, Local angle domain elastic reverse time migration in TI media: 76th Annual International Conference and Exhibition Incorporating SPE EUROPE, EAGE, Extended Abstracts, 752–756.

Wang, W., and G. A. McMechan, 2015, Vector-based elastic reverse time migration: Geophysics, **80**, no. 6, S245–S258, doi: 10.1190/geo2014-0620.1.

Wapenaar, C., N. Kinneging, and A. Berkhout, 1987, Principle of prestack migration based on the full elastic two-way wave equation: Geophysics, **52**, 151–173, doi: 10.1190/1.1442291.

Winterstein, D., 1990, Velocity anisotropy terminology for geophysicists: Geophysics, **55**, 1070–1088, doi: 10.1190/1.1442919.

Xie, X. B., and R. S. Wu, 2005, Multicomponent prestack depth migration using the elastic screen method: Geophysics, **70**, no. 1, S30–S37, doi: 10.1190/1.1852787.

Xu, S., Y. Zhang, and B. Tang, 2011, 3d angle gathers from reverse time migration: Geophysics, **76**, no. 2, S77–S92, doi: 10.1190/1.3536527.

Yan, J., and P. Sava, 2007, Elastic wavefield imaging with scalar and vector potentials: 77th Annual International Meeting, SEG, Expanded Abstracts, 2150–2154.

Yan, J., and P. Sava, 2008, Isotropic angle-domain elastic reverse-time migration: Geophysics, **73**, no. 6, S229–S239, doi: 10.1190/1.2981241.

Yan, J., and P. Sava, 2009, Elastic wave-mode separation for VTI media: Geophysics, **74**, no. 5, WB19–WB32, doi: 10.1190/1.3184014.

Yan, J., and P. Sava, 2012, Elastic wave mode separation for tilted transverse isotropic media: Geophysical Prospecting, **60**, 29–48, doi: 10.1111/j.1365-2478.2011.00964.x.

Yan, R., and X.-B. Xie, 2012, An angle-domain imaging condition for elastic reverse time migration and its application to angle gather extraction: Geophysics, **77**, no. 5, S105–S115, doi: 10.1190/geo2011-0455.1.

Yoon, K., and K. J. Marfurt, 2006, Reverse-time migration using the Poynting vector: Exploration Geophysics, **37**, 102–107, doi: 10.1071/EG06102.

Zhang, Q., and G. A. McMechan, 2010, 2D and 3D elastic wavefield vector decomposition in the wavenumber domain for VTI media: Geophysics, **75**, no. 3, D13–D26, doi: 10.1190/1.3431045.

Zhang, Q., and G. A. McMechan, 2011a, Common-image gathers in the incident phase-angle domain from reverse time migration in 2D elastic VTI media: Geophysics, **76**, no. 6, S197–S206, doi: 10.1190/geo2011-0015.1.

Zhang, Q., and G. A. McMechan, 2011b, Direct vector-field method to obtain angle-domain common-image gathers from isotropic acoustic and elastic reverse time migration: Geophysics, **76**, no. 5, WB135–WB149, doi: 10.1190/geo2010-0314.1.